

Modeling some “Meta” Aspects of Pore Growth in Semiconductors

H. Föll, M. Leisner, and J. Carstensen

Institute for Materials Science, Christian-Albrechts-University of Kiel,
Kaiserstrasse 2, D-24143 Kiel, Germany

A “meta” model for electrochemical pore growth in semiconductors is presented which is essentially based on two assumptions: i) current flow at the etching interface occurs in current bursts and not by constant current flow and ii) current flow depends on the passivation behavior at the etching interface. The meta model is thus not sensitive to factors like the semiconductor material or the detailed dissolution chemistry. In order to demonstrate the concept of the meta model a number of recent results in InP will be discussed. The treatise includes the mechanism of currentline and crystallographical pore growth, as well as the reasons for the characteristic transition between both pore growth modes. A numerical Monte Carlo model for pore growth based on the meta model, which is capable of closely simulating a number of pore structures, will also be presented.

Introduction

Electrochemically etched pores in semiconductors can be divided into two basic classes according to their appearance and properties: crystallographic pores (cristos) and currentline pores (curros). Both modes can be seen as extremes or paradigms of pore growth modes and there are many pores found somewhere in between these extremes (“curristos”). Crystallographic pores owe their name to their crystallographic growth direction, which is always the same independent of the sample’s surface orientation. Besides the basic growth direction other components of the pore geometry might show crystallographic features e.g. faceted pore tips or prismatic cross-sections. Currentline pores, on the other hand, grow perpendicular to the equipotential planes enveloping the pore tips. They thus usually grow perpendicular to the sample surface (except at the border or O-ring region), independent of the exact crystallographic orientation of the surface. In III-V semiconductors the division into cristo and curro pores is particularly relevant and widely accepted, since pores in these materials often show pure crystallographic or currentline behavior. Crysto pores have been etched into InP, GaAs, and GaP using a large assortment of electrolytes, cf. e.g. (1 - 11). Currentline pores have so far been found in InP and GaP (2, 12 - 16), again for a large variety of electrolytes. The classification can be easily extended to pores obtained in II-VI semiconductors (17, 18), which closely resemble the currentline pores found in InP, as well as to Si and Ge, where most pore types have always been of the cristo pore type (19 - 21), but currentline pore growth can also be obtained (22).

Since both pore types have been produced in nearly all semiconductors that are readily available in single-crystalline form, some meta principle that transcends detailed inter-

face chemistry and physics must govern pore growth on the meta level. In the concomitant meta model presented here we thus do not concern ourselves with “details”, e.g. which growth direction is the preferred one for cristo pores in some material, or what kind of chemical reactions take place at the interface. The basic assumption of the model is that current flow mostly proceeds in current bursts, i.e. is localized in space and time. This leads to the following meta features; all of which have been found to obtain at least in some circumstances; see (24) for details.

- i) The current (and the current density) in a single pore cannot be constant all the time; it “oscillates” with a stochastic component by necessity.
- ii) There is a probabilistic element in (cristo) pore growth that accounts for pore branching among other things.
- iii) The probability for a current burst (CB) strongly depends on the passivation of the considered surface element. Passivation in the conventional sense means that current flow at some fixed potential is more difficult through a passivated surface increment relative to an unpassivated one, e.g. through the formation of thin oxides or interface coverage by chemical species, and this definition is simply adopted to CBs. Note, however, that “passivation“ in this sense can also be due to non-chemical factors, i.e. reduced field strengths.
- iv) What happens for one pore is also influenced by its surroundings, i.e. by neighboring pores. They influence the local field strengths and thus current burst probabilities (and thus also the local hole density and supply).
- v) Correlations between neighboring pores via changed probabilities for CB’s is thus possible. This correlation may induce synchronization of growth modes and thus self-organization phenomena; cf. (23).

In what follows a selection of pore growth phenomena is presented, which will serve to illustrate the meta model. Most results presented here have been obtained on InP, which shows cristo and curro pores in full splendor, as has already been elaborated. A full treatise of the model is given in (24).

Currentline Pore Growth in the Framework of the Meta Model

Dependence on the Doping Level

Currentline pore growth on n-type InP is strongly dependent on the doping level N_D of the semiconductor. Figure 1 illustrates this statement by showing currentline pore structures for samples with $N_D = 1 \cdot 10^{17} \text{ cm}^{-3}$ in (a) cross-sectional view and (b) top view (after mechanical removal of the nucleation layer). Figure 1 (c) and (d) show the corresponding result for $N_D = 8 \cdot 10^{17} \text{ cm}^{-3}$ and (e) and (f) for $N_D = 3 \cdot 10^{18} \text{ cm}^{-3}$ (Note the higher magnification in (f)). The pores have a round shape that becomes more ellipsoid with decreasing N_D . The pore diameter is in the range of 130 nm for all three samples. Pores are arranged in a hexagonally close packed configuration. The pore wall thickness strongly deviates between the samples, it decreases with N_D .

It has been demonstrated in (25) by a combination of theoretical calculations and results from in-situ Fast-Fourier-Transform Impedance Spectroscopy (FFT IS), that the variation in pore wall thickness can be traced back to the existence of a space-charge-region (SCR) at the pore tips. The impossibility of overlapping the SCRs of adjacent pores consequently results in the N_D dependent minimum pore wall thickness obtained in the experiments.

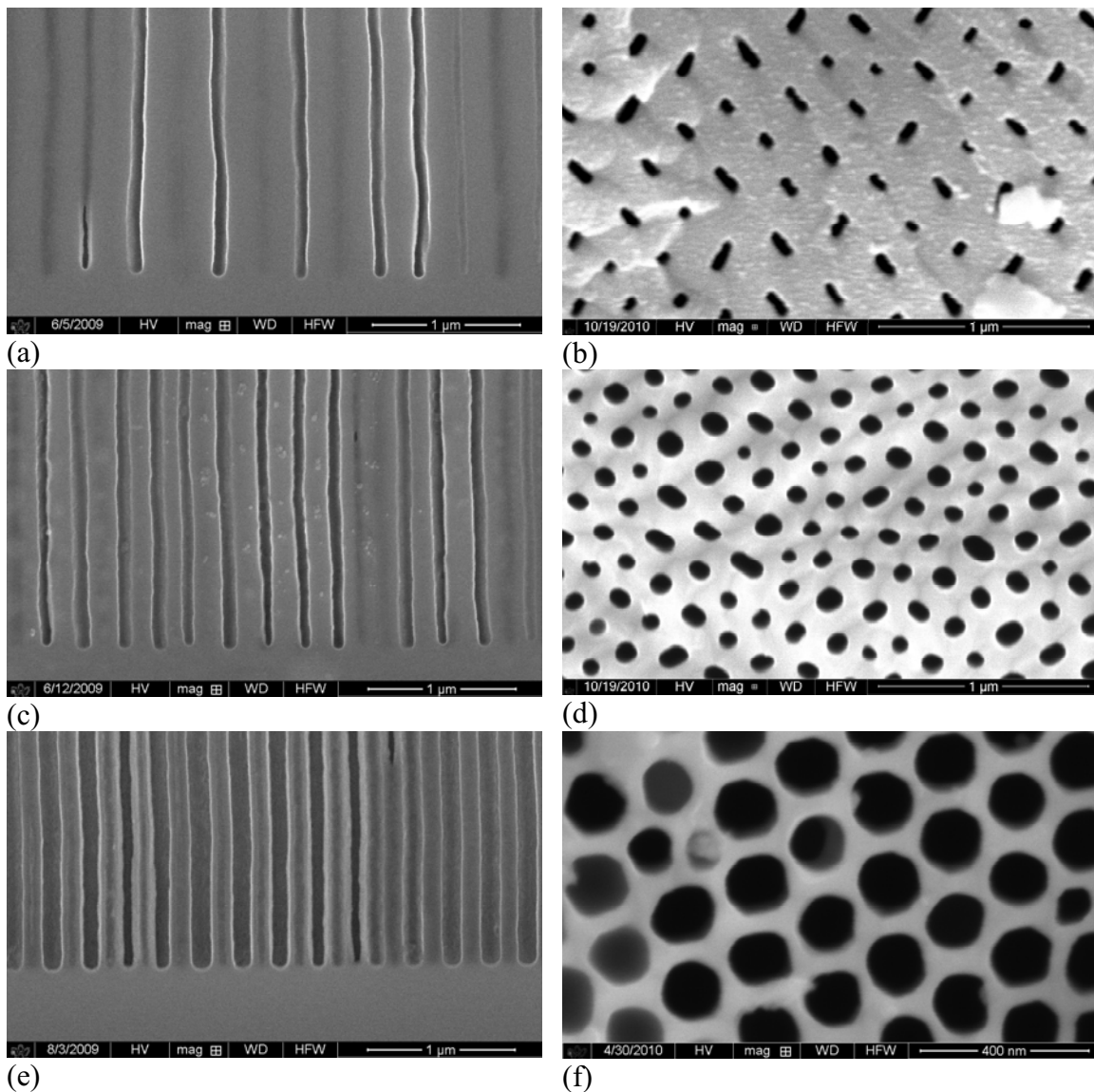


Figure 1. Currentline pores etched under optimized conditions for $N_D = 1 \cdot 10^{17} \text{ cm}^{-3}$ in (a) cross-sectional view and (b) plan view (after removal of the nucleation layer). (c) and (d) show the corresponding results for $N_D = 8 \cdot 10^{17} \text{ cm}^{-3}$, and (e) and (f) for $N_D = 3 \cdot 10^{18} \text{ cm}^{-3}$ (note the larger magnification in (f)).

Mass Transport

An essential process in the etching of currentline pores in InP is the transport of chemical species through the pores. This finding is especially important for the switch-over between pore growth modes, as will be shown here. Figure 2 shows the pore depth d_{pore} as function of the etching time t for several sets of experiments for samples with three different doping levels and at different constant etching potentials.

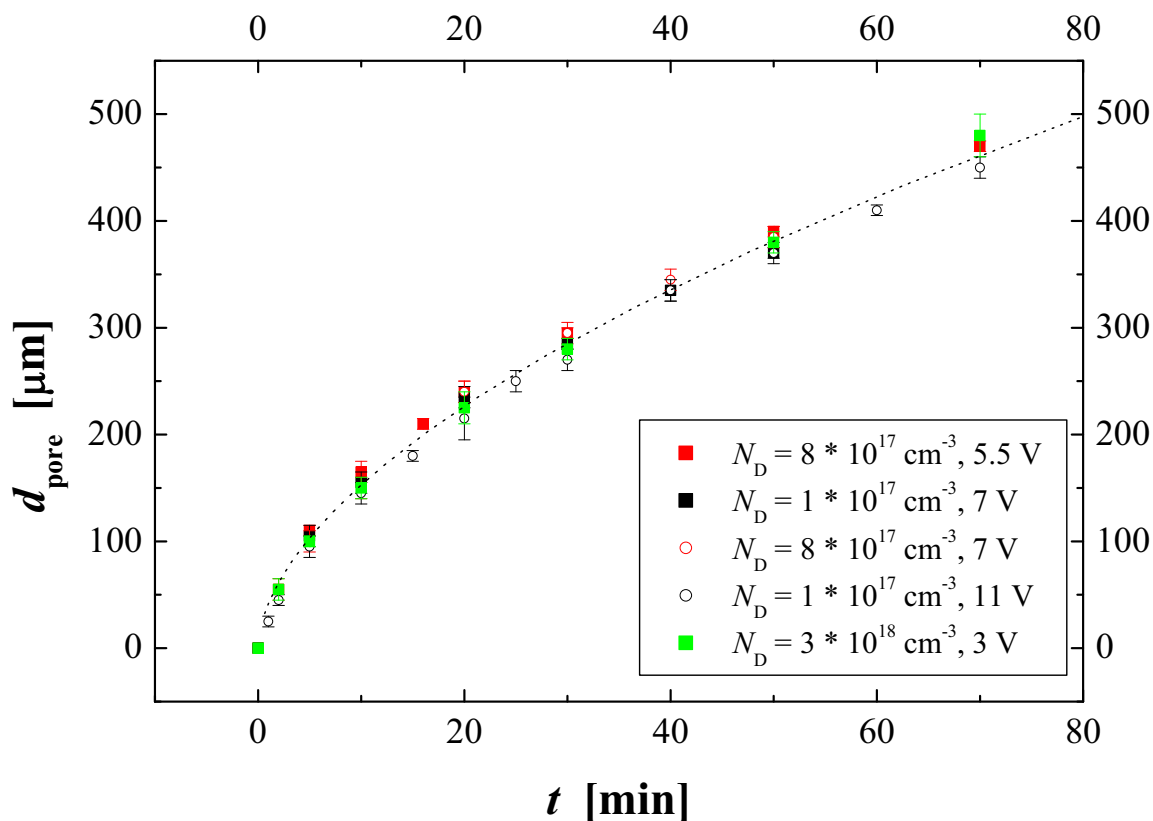


Figure 2. Chronological evolution of the pore depth d_{pore} of currentline pores etched in (100) n-type InP with different doping levels and for different constant etching potentials.

It can be observed that all experimental data (points) can be very well approximated by a potential growth law (dashed line) of the form

$$d_{\text{pore}} = d_0 \cdot t^\gamma, \quad [1]$$

with a pre-exponential factor $d_0 = 40.3 \mu\text{m}$ and an exponent $\gamma = 0.57$. Thus the etching velocity decreases significantly with increasing pore length, whereas the geometry of the pores, i.e. the pore diameter and shape of pore tips, are not altered throughout the experiment after the initial nucleation phase. This behavior can be consistently understood, if it is assumed that the mass transport through the pores is decisive. Another indication is the proximity of the exponent to 0.5, which is indicative of diffusional processes. The slight deviation might then be due to an additional drift component inside the pores due to the high potential drop inside the pores. This interpretation is also in agreement with results from the FFT IS analysis presented in (25). A more detailed treatment of equation [1] can be found in (22).

Crystallographic Pore Growth in the Framework of the Meta Model

Dependence on the Doping Level

The growth of crystallographic pores in InP depends on several experimental parameters. The doping concentration of the semiconductor has a very strong impact on the re-

sulting pore morphology. Figure 3 serves to illustrate this point. It shows a detail of the crystal pore morphology for pores etched in InP with the doping concentration of (a) $N_D = 1 \cdot 10^{17} \text{ cm}^{-3}$, (b) $N_D = 8 \cdot 10^{17} \text{ cm}^{-3}$, and (c) $N_D = 3 \cdot 10^{18} \text{ cm}^{-3}$, to highlight the differences and consistencies between these morphologies.

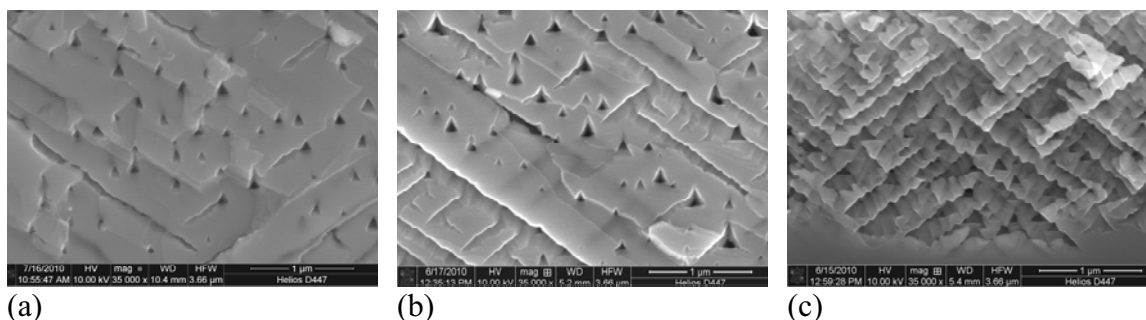


Figure 3. Detail of the crystal pore morphology obtained on (100) n-type InP with different doping concentrations. All experiments have been performed in galvanostatic mode with $j = 0.4 \text{ mA/cm}^2$ for 30 min and a 5 wt. % HCl electrolyte at $T = 20 \text{ }^\circ\text{C}$. (a) $N_D = 1 \cdot 10^{17} \text{ cm}^{-3}$, (b) $N_D = 8 \cdot 10^{17} \text{ cm}^{-3}$, and (c) $N_D = 3 \cdot 10^{18} \text{ cm}^{-3}$, respectively.

Crystal pores appear in two ways: as lengthy channels, which represent downward growing pores and as triangles, representing upward growing crystal pores that intersect the cleavage plane observed. A thorough analysis of the obtained data yields a decreasing layer thickness, a closer packing of pores (higher pore density), as well as bigger pore sizes with increasing doping level N_D .

The dependency of the minimum distance between pores on the doping level N_D can be easily understood, if the presence of a SCR around the pore walls is assumed, which would define an impenetrable barrier for the growing pore tip. Since the SCR width depends on $N_D^{-1/2}$, the pores can get closer packed with increasing N_D . A more detailed investigation (not shown here) of the chronological evolution of the pore morphology furthermore reveals that the branching frequency increases with increasing N_D . In the framework of the meta model this phenomenon can be understood via a coupling of current burst probabilities to N_D . The physical reason for increased “passivation” with decreasing N_D is the coupling of field strength to the SCR width. How pore branching and CB probabilities are connected will become clear in the next paragraph.

3-Dimensional Monte-Carlo-Simulation of Crystal Pore Growth

As elaborated in the introduction, the meta model for pore growth describes the branching at pore tips and pore walls as a probability process. This stochastic nature of the meta model allows to implement it in a Monte-Carlo-simulation. In this part of the manuscript, the principle of the simulation will be briefly explained, and a comparison of experimental and simulation results will subsequently be presented.

The simulation has been performed on a simulation array of the size $(1024 \cdot 1024 \cdot 1024)$ voxels. The uppermost layer of this array represents the (100)-oriented surface of the InP sample. Accordingly, the two diagonal planes of the cube that are furthermore perpendicular to the surface represent $(1\bar{1}0)$ and (110) planes, in which the crystal pores grow. A schematic illustration of the $(1\bar{1}0)$ plane is given in Fig. 4 (a), in which downward growing pores are illustrated in red colors, whereas upward growing pores, which

are intersecting the plane of view, are drawn in blue colors. Branching at a pore tip can occur, as is evident from the chronological evolution of the pore morphology. Branching out of pore walls can also occur, but is not directly visible since the freshly generated pore tip grows out of resp. into the plane of view. These branching events then are represented by a darker color of these voxels. In each iteration the simulation array will be transformed into a new state according to the following rules:

1. Each pore tip grows on for one more voxel into its respective pore growth direction and the former pore tip becomes a pore wall.
2. Growth (and also branching) can only occur, if there is free space in the new growth direction. If there are any pores present in an (adjustable) distance l_{free} from the pore tip, the pore will stop to grow.
3. Pores can branch at the pore tips (see $(m+1)$ -th iteration). The new pore will also grow downwards. The probability k_{tips} for branching at a tip per iteration is proportional to the current density at the pore tips j_{tips} and to a branching parameter p_{tips} , which is the first free input parameter of the simulation.
4. Pores can also branch out of the pore walls (see dark red voxels in the red pore in $(m+2)$ -th iteration). The new pore will be an upward growing pore, growing out of the $(1\bar{1}0)$ plane. The probability for branching out of walls per iteration k_{walls} is proportional to the current density at the pore tips j_{tips} and to a branching parameter p_{walls} , which is the second free input parameter.
5. If two pore tips meet in one voxel, one tip will continue to grow, whereas the other one will stop to grow.
6. If branching has occurred at one voxel, no branching can occur out of the neighboring voxels, which will be set to an “inactive” pore wall state (darker color). The number of affected neighbor voxels can be adjusted by the parameter l_{pass} .

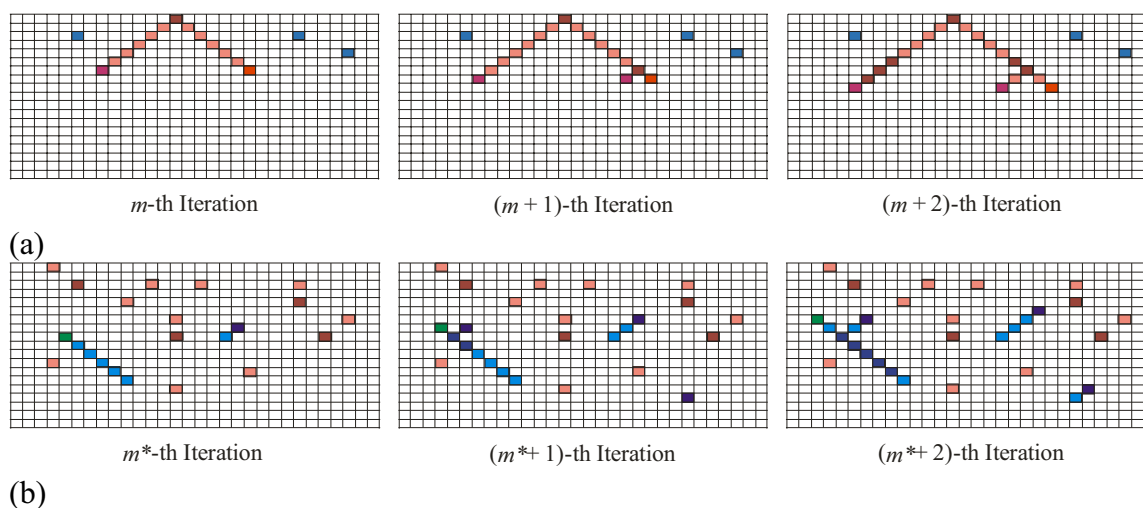


Figure 4. Schematic representation of crystal pore growth in the simulation array. (a) View of the $(1\bar{1}0)$ plane, in which downward growing pores are situated (red voxels), whereas upward growing pores (blue) are intersecting the plane. Branching at pore tips and out of pore walls can occur. (b) View of the (110) plane, in which upward growing pores are blue chains of voxels, whereas downward growing pores (red) are intersecting the plane. Branching at pore tips and out of pore walls can analogously occur.

Analogously, the same branching events are also possible for the upward growing pores. These pores grow in the (110) plane, as is schematically illustrated in Fig. 4 (b),

and are illustrated in blue colors. The downward growing pores, shown in red, are intersecting the plane of view. Branching at pore tips and walls can again be identified from the chronological evolution.

Before the simulation can start, a pre-defined density of pores will be randomly put into the topmost layer of the simulation array, thus constituting the “nucleation layer” of the simulation.

Figure 5 shows the result of a simulation of the crystal pore morphology obtained on InP with a doping concentration $N_D = 8 \cdot 10^{17} \text{ cm}^{-3}$. In the two left columns the whole layer is compared for three different etching times (the nucleation layer has been removed in the SEM images). In the two right columns a detail of the pore morphology is shown at constant magnification for the same three etching times. The simulation has been performed with the branching parameters set to $p_{\text{tips}} = 5 \text{ cm}^2/\text{mA}$ and $p_{\text{walls}} = 50 \text{ cm}^2/\text{mA}$. As secondary parameters the array mesh size $d_{\text{mesh}} = 100 \text{ nm}$ was adjusted to the experimentally determined crystal pore diameter (i.e. the triangle side length). The current j was set to $0.4 \text{ mA}/\text{cm}^2$ and the starting etching velocity v_{start} to $1.2 \text{ }\mu\text{m}/\text{min}$, just as in the electrochemical experiment. The nucleation tip density ρ_{nucl} was set to $1 \text{ }\mu\text{m}^{-2}$. The free length parameter l_{free} was set to 0 voxels and the passivation length to $l_{\text{pass}} = 2$ voxels.

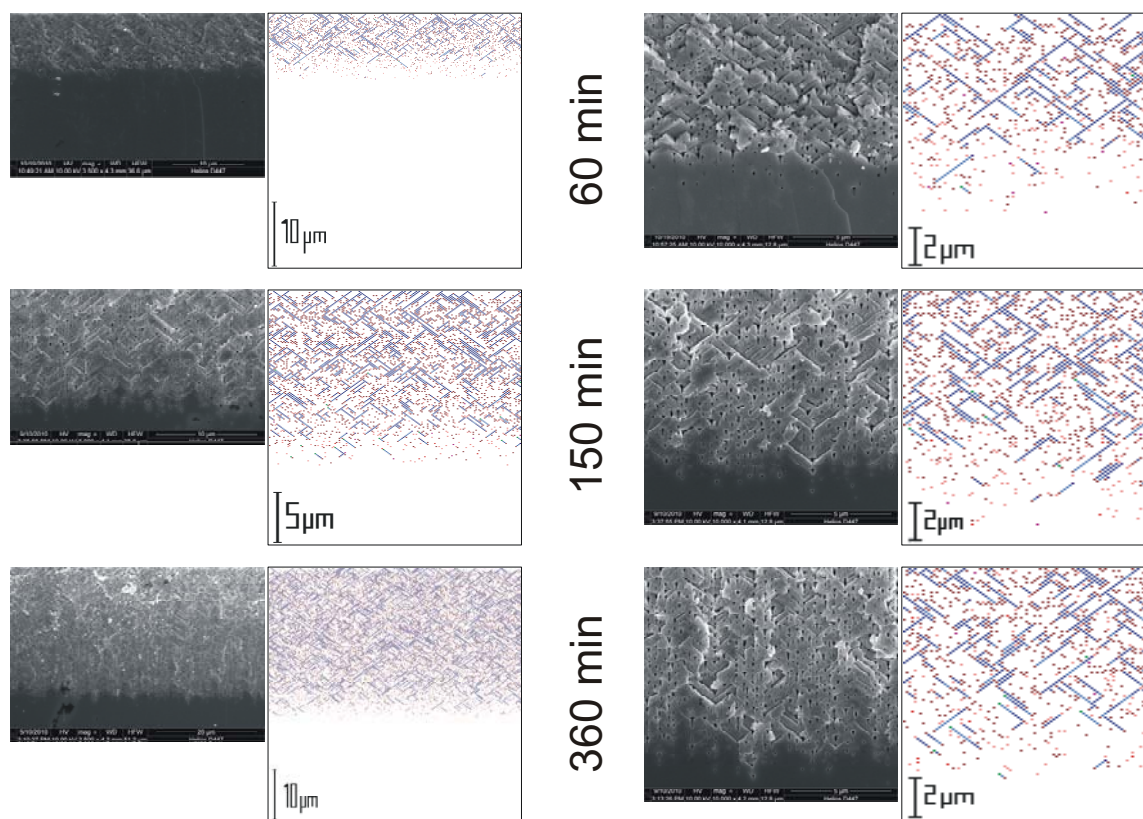


Figure 5. Comparison of the etched and simulated crystal pore morphology on InP with a doping concentration of $N_D = 8 \cdot 10^{17} \text{ cm}^{-3}$ in the (110) plane for three different etching times. The two leftmost columns show a comparison of the whole crystal layer, the two rightmost columns a detail of the structure at same magnification.

The simulated pore morphology reproduces the experimental results very well, as is already evident from Fig. 5. Fig. 6 gives more quantitative numbers from the simulation, points always represent the experimental results, whereas simulation results are given by

lines. In Fig. 6 (a) the pore density ρ_{pore} of upward growing pores as a function of depth d is shown for three different etching times. Fig. 6 (b) shows the corresponding result for the downward growing pores. Fig. 6 (c) depicts the chronological evolution of the pore depth d_{pore} . All simulation results agree again very well with the experimental data.

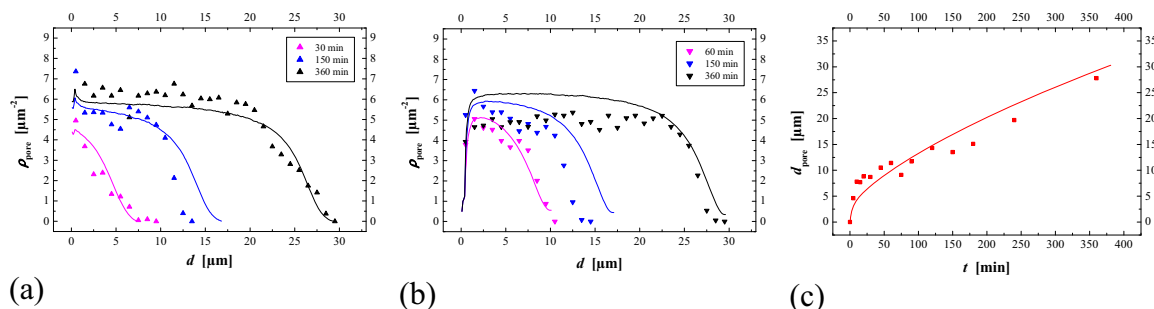


Figure 6. Simulation results (lines) in comparison to experimental data (points) for InP with $N_{\text{D}} = 8 \cdot 10^{17} \text{ cm}^{-3}$. (a) Pore density ρ_{pore} of upward growing pores as a function of depth d for three etching times. (b) Analogous results for the downward growing pores. (c) Chronological evolution of the pore depth d_{pore} .

The obvious question remaining considers the physical nature of the branching probability. As mentioned before, the branching probabilities reflect the different passivation behavior of crystallographic planes, in the framework of the meta model presented here. In this vein it is also possible to understand the dependence on the doping level of the semiconductor, which yields weaker passivation for increasing N_{D} due to a reduction in the SCR width. Accordingly the differences of crystal pore growth in different materials can also be understood, as has been elaborated in (24), by different intrinsic passivation behavior.

Switch-Over between the Pore Growth Modes

Externally Induced Switch-Over

It has been stressed that the main difference between currentline and crystallographic pore growth is the state of passivation of the pores. The necessary deficiency of passivating species during currentline pore growth is usually established by mass transfer limitations in the pores because fast growing pores at high external potential / currents use up the species in question as fast as it arrives, reducing the concentration at the pore tip region to essentially zero. If the potential / current is externally reduced or switched-off for some time, the relevant species concentration inside the pores should be able to relax into a state that allows for significant passivation, i.e. differences of passivation for crystallographic planes appear. Hence, the pore growth mode should switch to crystallographic pore growth. This predicted behavior is in fact observed, as Fig. 7 demonstrates. It shows a pore double layer, where the initial currentline pores have been grown at comparatively high external potential / current density. After a significant decrease of the potential / current density, the pore growth mode changes to crystallographic pore growth in the bottom layer. The crystallographic nature of these pores becomes directly apparent in the (100) samples shown in Fig. 7 (a) while the changeover in the (111) sample of Fig. 7 (b) is more subtle and might be missed.

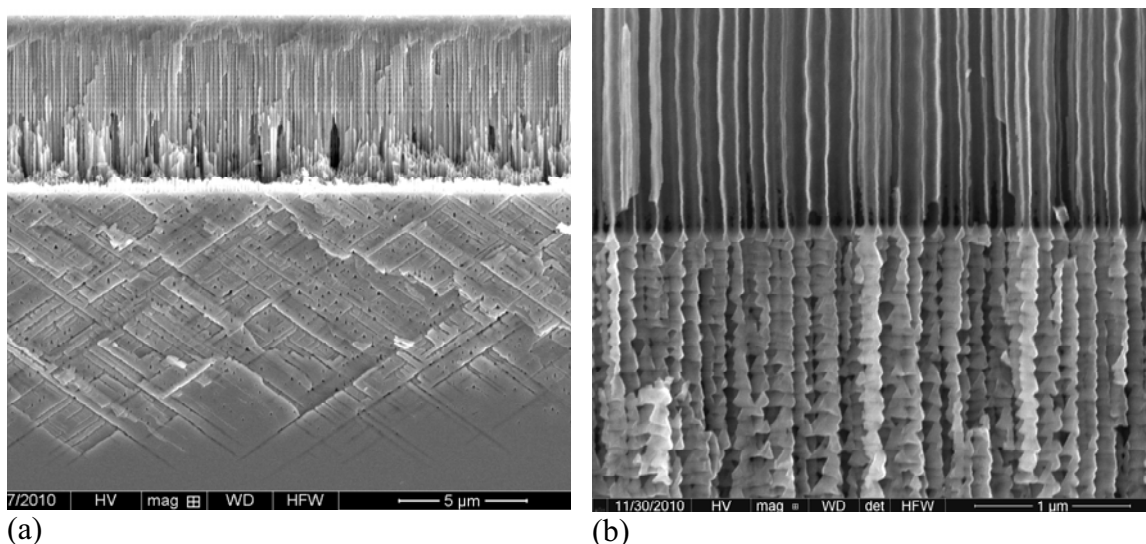


Figure 7. Externally induced switch-over from currentline pore growth to crystallographical pore growth in (a) (100)-oriented n-type InP with a doping level of $N_D = 8 \cdot 10^{17} \text{ cm}^{-3}$ and (b) (111)-oriented n-type InP with $N_D = 1 \cdot 10^{18} \text{ cm}^{-3}$.

Self-Induced Switchover

Besides the possibility of externally switching the pore growth mode, a self-induced switchover from cristo to curro pore growth is expected within the framework of the meta model. If a cristo pore layer gets thicker, at some point in time the length of the pores should be large enough to limit the mass transfer of chemical species through the pores to the pore tips below some critical values where $\{hkl\}$ -dependent passivation becomes irrelevant and cristo pore growth can no longer be maintained. This predicted self-induced switchover indeed occurs. Fig. 8 presents the resulting pore morphologies after the switchover for the three analyzed doping levels. On a first view the pores look neither like curro nor like cristo pores, but like something in between, and have thus been labeled as “curristo” pores. These pores are roundish and do not possess crystallographic pore walls and tips. The growth direction is not tied to crystallography. Bunches of pores grow roughly spherically from individual starting areas, yielding a non-planar pore front.

Curristo pores thus preserve the main features of currentline pores, the only missing ingredient is the close-packed ordering observed during “ideal” curro pore growth, cf. Fig. 1. The appearance of only curristo pores after a self-induced switchover can be also easily grasped within the framework of the meta model. Even though mass transport is limited, as required for curro pore growth, there is neither a large external potential nor a large current in this case in contrast to the case of externally enforced “proper” curro pores. The current density at the tips of curristo pores is thus relatively small. Since the meta model considers current to flow in current bursts, this translates into a lower burst frequency, i.e. one pore may grow arbitrarily into free space because neighboring pores do not restrict its growth direction. In contrast, for close-packed rapidly growing “proper” curro pores, the current burst frequency is so high by necessity that nearly all pores grow at any time and SCRs surrounding the pore tips prevent pore growth out of the “straight” growth direction of pores.

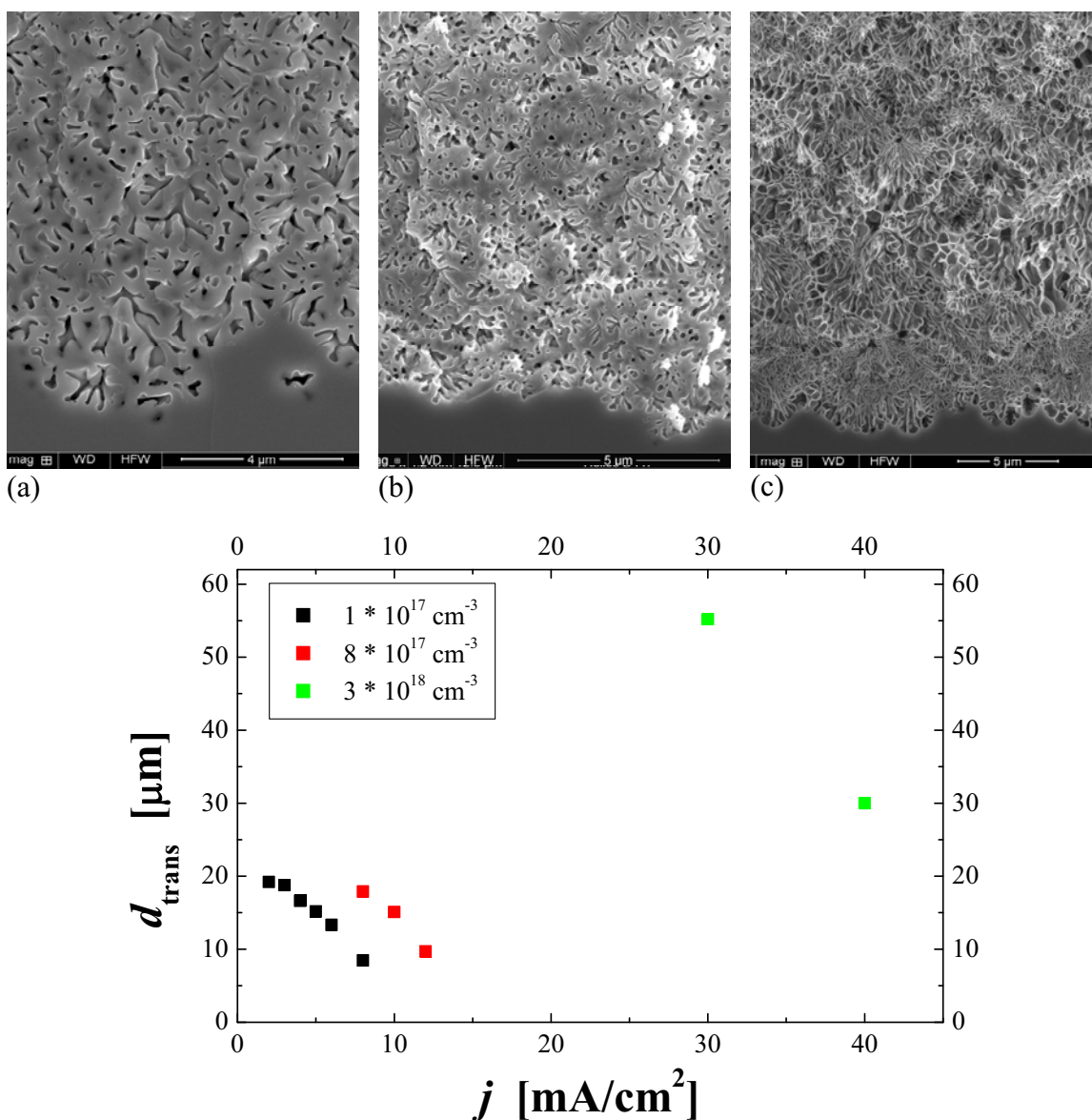


Figure 8. Curristo pores in (100) n-type InP obtained after etching for 30 minutes under galvanostatic conditions. (a) $N_D = 1 \cdot 10^{17} \text{ cm}^{-3}$, $j = 5 \text{ mA/cm}^2$, (b) $N_D = 8 \cdot 10^{17} \text{ cm}^{-3}$, $j = 8 \text{ mA/cm}^2$, and (c) $N_D = 3 \cdot 10^{18} \text{ cm}^{-3}$, $j = 40 \text{ mA/cm}^2$, respectively. (d) Curristo pores occur at the transition depth d_{trans} , which is dependent on the semiconductor doping level, as well as the etching current density j .

This interpretation also explains the dependence of the transition depth d_{trans} at which the self-induced cristo-curristo switchover occurs. It occurs at higher depth for higher doping level N_D , as well as for higher current densities j . The latter dependency is rather obvious, since the higher current consumes Cl^- species, which are also believed to be the main passivating species for III-V semiconductors. The dependency on N_D is also understandable, since the cristo pore morphology which laterally precedes the curristo pore layer, is much more porous, as has been elaborated earlier (see Fig. 3), and thus constitutes a much smaller diffusion barrier.

Conclusion

It has been demonstrated that a simple meta model based on the passivation behavior of the semiconductor-electrolyte interface is able to explain the basic differences between the currentline and crystallographic pore growth modes, as well as the characteristic switch-over behavior between the two modes. Currentline pores essentially grow if the passivation at the pore tips gets very weak, i.e. it is nearly not impeding current flow through the interface. This condition can be obtained if the supply of chemical species through the elongating pores is becoming limiting, a condition that can be forced by applying high external potentials. Contrastingly, crystallographic pore growth requires strong passivation, such that differences in the passivation of crystallographic planes become important, yielding the characteristic crystallographic appearance of these pores. The differences in passivation between pore tips and walls, between different semiconductors, and for material with different doping level express themselves in differing branching probabilities, as has been demonstrated through a three-dimensional Monte-Carlo-simulation of cristo pore growth.

References

1. T. Takizawa, S. Arai, and M. Nakahara, *Japan J. Appl. Phys.* **33(2, 5A)**, L643 (1994).
2. H. Föll, S. Langa, J. Carstensen, S. Lölkes, M. Christophersen, and I.M. Tiginyanu, *Adv. Mater.* **15(3)**, 183 (2003).
3. Z. Weng, W. Zhang, C. Wu, H. Cai, C. Li, Z. Wang, Z. Song, and A. Liu, *Appl. Surf. Sci.* **256(7)**, 2052 (2010).
4. C. O'Dwyer, D.N. Buckley, D. Sutton, and S.B. Newcomb, *J. Electrochem. Soc.* **153(12)**, G1039 (2006).
5. O. Volciuc, E. Monaico, M. Enachi, V.V. Ursaki, D. Pavlidis, V. Popa, and I.M. Tiginyanu, *Appl. Surf. Sci.* **257(3)**, 827 (2009).
6. J. Wloka and P. Schmuki, *J. Electroceram.* **16(1)**, 23 (2006).
7. Y.C. Shen, M.H. Hon, I.C. Leu, and L.G. Teoh, *Appl. Phys. A* **98(2)**, 429 (2010).
8. K. Müller, J. Wloka, and P. Schmuki, *J. Solid State Electrochem.* **13(5)**, 807 (2009).
9. I.M. Tiginyanu, V.V. Ursaki, E. Monaico, E. Foca, and H. Föll, *Electrochem. and Sol. State Lett.* **10(11)**, D127 (2007).
10. F.M. Ross, G. Oskam, P.C. Searson, J.M. Macaulay, and J.A. Liddle, *Phil. Mag. A* **75(2)**, 525 (1997).
11. R.W. Tjerkstra, J. Gómez-Rivas, D. Vanmaekelbergh, and J.J. Kelly, *Electrochem. Solid State Lett.* **5(5)**, G32 (2002).
12. E. Kikuno, M. Amiotti, T. Takizawa, and S. Arai, *Japan J. Appl. Phys.* **34(1, 1)**, 177 (1995).
13. A. Hamamatsu, C. Kaneshiro, H. Fujikura, and H. Hasegawa, *J. Electroanal. Chem.* **473**, 223 (1999).
14. A. Liu, *Nanotechnology* **12**, L1 (2001).
15. P. Schmuki, U. Schlierf, T. Herrmann, and G. Champion, *Electrochim. Acta* **48**, 1301 (2003).
16. L. Santinacci, A.-M. Goncalves, N. Simon, and A. Etcheberry, *Electrochim. Acta* **56(2)**, 878 (2010).

17. E. Monaico, V.V. Ursaki, A. Urbieto, P. Fernández, J. Piqueras, R.W. Boyd, and I.M. Tiginyanu, *Semicond. Sci. Technol.* **19(12)**, L121 (2004).
18. E. Monaico, I.M. Tiginyanu, V.V. Ursaki, A. Saruna, M. Kuball, D.D. Nedeoglo, and V.P. Sirkeli, *Semicond. Sci. Technol.* **22**, 1115 (2007).
19. V. Lehmann, *Electrochemistry of Silicon*, Wiley-VCH, Weinheim (2002).
20. H. Föll, M. Leisner, A. Cojocaru, and J. Carstensen, *Materials* **3**, 3006 (2010).
21. C. Fang, H. Föll, and J. Carstensen, *J. Electroanal. Chem.* **589**, 259 (2006).
22. A. Cojocaru, M. Leisner, J. Carstensen, and H. Föll, *Phys. Stat. Sol. (c)* (in print) (2011).
23. H. Föll, M. Leisner, A. Cojocaru, and J. Carstensen, *Electrochim. Acta* **55(2)**, 327 (2009).
24. M. Leisner, H. Föll, and J. Carstensen, "A meta model for electrochemical pore growth in semiconductors", in *Nanostructured semiconductors: from basic research to applications*, ed. P. Granitzer, Springer (2011).
25. M. Leisner, J. Carstensen, and H. Föll, *Phys. Stat. Sol. (a)* (in print) (2011).